



One-pot synthesis of monodisperse palladium–copper nanocrystals supported on reduced graphene oxide nanosheets with improved catalytic activity and methanol tolerance for oxygen reduction reaction

Jing-Jing Lv^a, Shan-Shan Li^a, Ai-Jun Wang^a, Li-Ping Mei^a, Jiu-Ju Feng^{a,*},
Jian-Rong Chen^a, Zhaojiang Chen^{b,*}

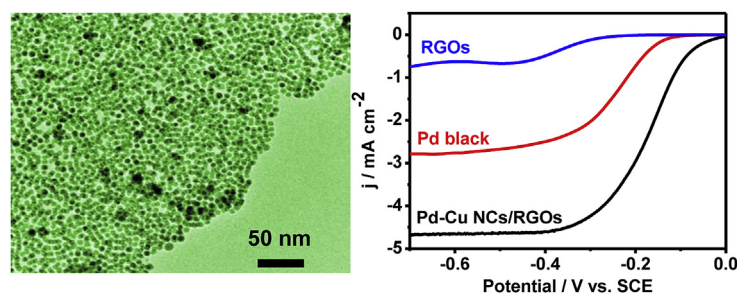
^a College of Geography and Environmental Science, College of Chemistry and Life Science, Zhejiang Normal University, Jinhua 321004, China

^b Department of Physics, Zhejiang Normal University, Jinhua 321004, China

HIGHLIGHTS

- Monodisperse Pd–Cu NCs/RGOs are fabricated by a one-pot solvothermal strategy.
- This method is facile, convenient, and efficient, without using any seed or template.
- The Pd–Cu NCs/RGOs possess the enlarged electrochemically active surface area.
- The nanocomposites exhibit high electrocatalytic activity and remarkable methanol tolerance toward ORR in alkaline media.

GRAPHICAL ABSTRACT



ARTICLE INFO

Article history:

Received 10 May 2014

Received in revised form

5 July 2014

Accepted 5 July 2014

Available online 11 July 2014

Keywords:

Bimetallic nanocrystals

Reduced graphene oxide

Oxygen reduction reaction

Methanol tolerance

ABSTRACT

Monodisperse bimetallic alloyed palladium–copper nanocrystals are uniformly supported on reduced graphene oxide nanosheets by a one-pot solvothermal strategy, with an average size of 6.81 nm. As a result, the as-prepared nanocomposites have the enlarged electrochemically active surface area ($49.2 \text{ m}^2 \text{ g}^{-1}$), and display the improved electrocatalytic performance and high methanol-tolerance ability for oxygen reduction reaction in alkaline media, compared with commercial Pd black and RGOs. Those RGOs-supporting Pd–Cu alloys would have potential applications in fuel cells.

© 2014 Elsevier B.V. All rights reserved.

1. Introduction

Noble metal nanocrystals (NCs) are considered as promising catalysts in fuel cells [1,2]. Among them, Pt and Pd-based nanostructures are of central significance in catalyzing the anode and/or cathode reactions in fuel cells [3–5]. Compared with Pt, Pd has many intrinsic advantages such as lower cost and almost no

* Corresponding authors. Tel./fax: +86 579 82282269.

E-mail addresses: jjfeng@zjnu.cn, jjfengnju@gmail.com (J.-J. Feng), zjchen@zjnu.cn (Z. Chen).

CO-poisoning effects [6,7]. Moreover, Pt-based catalysts suffer from slow kinetics of oxygen reduction reaction (ORR) resulted from a huge overpotential (400 mV), which severely limits the overall performance of fuel cells [8]. Therefore, it would be interesting and important to develop non-Pt NCs, while maintaining high catalytic activity.

Generally, Pd-based nanocatalyst is an ideal alternative to replace Pt, which has a high electrocatalytic activity toward ORR in alkaline media [9,10]. Last decades have witnessed the emergence of various Pd-based nanomaterials and their wide applications [11–15]. For instance, Yin and co-workers prepared Pd-alloyed (Pd–Co and Pd–Cu) nanoparticles with enhanced catalytic activity for ethanol oxidation. Xiao' group found that there is a strong dependence of Pd activity on its morphology toward ORR [16]. Despite these demonstrations, it is still of practical importance to develop novel Pd-based catalysts with enhanced catalytic performance for the progress of fuel cells.

As known, the shape, size, and distribution of metallic NCs are the key factors to determine their properties [17]. Their synthesis is believed to be crucial for searching nanomaterials with novel properties [18,19]. Besides, bimetallic nanostructures own more remarkable catalytic performances over monometallic counterparts [16,20]. Hence, alloying Pd with other less expensive transition metals is a potential way to enhance the catalytic activity, along with reduce the cost [21].

Meanwhile, suitable carbon-based supports are also important to disperse metallic NCs, which is another strategy to improve the catalytic activity and reduce the cost [22,23]. As one of oxygen-abundant carbon layered materials, graphene has attracted continually attention after its discovery in 2004 [24], which has been extensively applied as a good support for catalysts, owing to its higher electrical conductivity and larger surface area ($2600 \text{ m}^2 \text{ g}^{-1}$) [25,26].

In this study, a facile and efficient solvothermal strategy was developed for preparation of bimetallic alloyed Pd–Cu NCs supported on reduced graphene oxygen nanosheets (denoted as Pd–Cu NCs/RGOs). The catalytic activity of Pd–Cu NCs/RGOs was investigated for ORR, using commercial Pd black and RGOs as references.

2. Experimental

2.1. Chemicals

Palladium(II) acetylacetonate ($\text{Pd}(\text{acac})_2$), copper acetylacetonate ($\text{Cu}(\text{acac})_2$), poly(vinylpyrrolidone) (PVP, MW = 58000), formaldehyde, ethylene glycol (EG), 1-hexadecyl-2,3-dimethylimidazolium bromide ($[\text{C}_{16}\text{MMIm}]\text{Br}$), and commercial Pd black were supplied from Shanghai Aladdin Chemical Reagent Company (Shanghai, China). All the other reagents were analytical grade and used without further purification. All aqueous solutions were prepared with twice-distilled water throughout the whole experiments.

2.2. Instrumentations

The morphology, composition, and metal distribution of the samples were observed by transmission electron microscopy (TEM), high-resolution TEM (HRTEM), X-ray energy dispersive spectroscopy (EDS), and high angle annular dark field-scanning transmission electron microscopy (HAADF-STEM) on a JEM-2100F transmission electron microscope coupled with an energy-dispersive X-ray spectrometer. TEM analysis was carried out at an accelerating voltage of 200 kV, and Mo grid was used as a substrate. A small amount of the sample was dispersed in ethanol after ultrasonication, and then a drop of the suspension was deposited on the Mo grid for TEM observation. The crystal structures were

conducted by X-ray diffraction (XRD) spectroscopy using a Bruker-D8-AXS diffractometer system equipped with $\text{Cu K}\alpha$ radiation. The X-ray photoelectron spectroscopy (XPS) was conducted on a K-Alpha XPS spectrometer using $\text{Al K}\alpha$ X-ray radiation (1486.6 eV) for excitation. Raman spectra were tested on a Renishaw Raman system model 1000 spectrometer equipped with a charge-coupled device (CCD) detector. Thermogravimetric analysis (TGA) was performed under a flow of air on a NETZSCH STA 449C analyzer and the samples were heated from 25 to 900°C with a heat rate of $10^\circ\text{C min}^{-1}$.

2.3. Preparation of Pd–Cu NCs/RGOs

Pd–Cu NCs/RGOs were synthesized as follows. Firstly, GOs were prepared by the modified Hummer's method [27]. Then, 0.1 g $\text{Pd}(\text{acac})_2$ and 0.086 g $\text{Cu}(\text{acac})_2$ were put into 15 mL EG, which contains 5 mM GOs, 0.32 g PVP, and 0.201 g ($[\text{C}_{16}\text{MMIm}]\text{Br}$). The mixed solution was stirred for 1 h at room temperature to obtain a homogeneous suspension. Next, the mixture was transferred into a 25 mL Teflon-lined stainless-steel autoclave and heated at 160°C for 6 h. Then, the autoclave was cooled to room temperature naturally. The final black precipitate was collected by centrifugation, thoroughly washed with ethanol and water to remove the residual PVP and ($[\text{C}_{16}\text{MMIm}]\text{Br}$), and dried at 60°C in vacuum for characterization.

2.4. Electrochemical measurements

All electrochemical experiments were performed on a CHI 660D electrochemical workstation (CH Instruments, Chenhua Company, Shanghai, China), and conducted on a conventional three-electrode cell, including a platinum wire as the counter electrode, a saturated calomel electrode (SCE) as the reference electrode, and the bare or modified glassy carbon electrode (GCE, 3 mm in diameter) or rotating disk electrode (RDE, 4 mm in diameter) as the working electrode.

For typical fabrication of Pd–Cu NCs/RGOs modified electrode, 2 mg of the sample was put into 1 mL water and dispersed by ultrasonication for 30 min to obtain a homogeneous suspension (2 mg mL^{-1}). Next, 6 and 15 μL of the suspension were homogeneously casted on the clean GCE and RDE, respectively, followed by casting another layer of Nafion (0.05 wt %) on the electrode surfaces to seal the samples in place and dried in air. The specific loading of the catalysts on the GCE and RDE were 0.17 mg cm^{-2} and 0.24 mg cm^{-2} , respectively. For comparison, commercial Pd black and RGOs modified GCE and RDE were prepared in a similar way.

To measure the electrochemically active surface area (ECSA) of Pd–Cu NCs/RGOs and Pd black modified electrodes, electrochemical CO-stripping voltammograms were obtained by oxidizing pre-adsorbed CO (CO_{ad}) in 0.5 M H_2SO_4 at a scan rate of 50 mV s^{-1} . CO was bubbled through the electrolyte for 20 min to allow complete adsorption of CO onto the deposit. The amount of the CO_{ad} was evaluated by integrating the CO_{ad} stripping peak and correcting for the capacitance of the double electric layer. Besides, the cyclic voltammetric experiments were performed in 0.1 M KOH + 3.0 M methanol at a scan rate of 50 mV s^{-1} to test the methanol-tolerance activity. Meanwhile, their corresponding ORR measurements were performed with a Model 616 rotating disk electrode. All the experiments were performed at room temperature, if not stated otherwise.

3. Results and discussion

Fig. 1A shows TEM image of the typical product. The product contains numerous spherical nanoparticles evenly dispersed on

RGOs with high density. HAADF-STEM image (Fig. 1B) further illustrates uniform distribution of metallic Pd–Cu NCs on RGOs surfaces, owing to the capping roles of PVP and $[\text{C}_{16}\text{MIM}]\text{Br}$ [28]. The corresponding elemental mapping images prove homogeneous distribution of Pd and Cu elements in each nanoparticle (Fig. 1C, D), revealing the formation of Pd–Cu alloys [29]. The EDS line scanning profiles indicate that the amount of Pd is about 3 times higher than that of Cu (Fig. 1E), as strongly supported by EDS data (Fig. 1F). This is due to much higher standard reduction potential of Pd^{2+}/Pd with 0.92 V versus reversible hydrogen electrode (vs. RHE) than that of Cu^{2+}/Cu (0.34 V, vs. RHE).

Notably, well-dispersed Pd–Cu nanoparticles are almost uniform in size (Fig. 2A), as demonstrated by the associated size distribution diagram (inset in Fig. 2A). Besides, the average size of Pd–Cu NCs is around 6.81 nm, which is considered to be favorable for enlarging their surface area, thereby improving their catalytic activity [30]. Meanwhile, the lattice spacing is about 0.22 nm in different marked positions (Fig. 2B), which can be assigned to the (111) planes of the face-centered cubic (fcc) Pd–Cu, further revealing the formation of Pd–Cu alloys [31]. Additionally, polycrystalline nature of Pd–Cu NCs is manifested by the corresponding selected-area electron diffraction (SAED) pattern (inset in Fig. 2B) [32].

The crystalline structures of Pd–Cu NCs/RGOs were examined by XRD spectrum (Fig. 3A). The representative diffraction peaks located at 40.9° , 47.1° , 69.4° and 83.4° are assigned to the (111), (200), (220), and (311) planes of the fcc Pd–Cu [25,33]. Impressively, these peaks are located between bulk Pd (JCPDS-46-1043) and Cu (JCPDS-04-0836), confirming the formation of Pd–Cu alloys [34]. Besides, the diffraction peak emerged at 35.3° corresponds to the (100) planes of CuO, verifying the existence of Cu oxidation state in Pd–Cu NCs [35]. Moreover, the peak at 23.2° is the characteristic peak of the (002) planes for RGOs, indicating the efficient reduction of GOs [22,36].

The effective reduction of GOs can be further manifested by Raman spectroscopy, which is an effective tool to characterize carbon-based materials [37]. Raman spectra of Pd–Cu NCs/RGOs (Fig. 3B, curve a) and GOs (Fig. 3B, curve b) both exhibit two prominent peaks, corresponding to well-documented D and G bands. The D band is associated with the vibrations of the sp^3 carbon atoms of disordered graphene nanosheets, while the G band is related to the vibrations of sp^2 carbon atom domains of graphite [6]. The D/G peak intensity ratio (I_D/I_G) is usually applied to evaluate the graphitization degree [38]. The I_D/I_G is around 1.05 for Pd–Cu NCs/RGOs, which is larger than that of GOs (0.94), strongly proving the efficient reduction of GOs to RGOs [34].

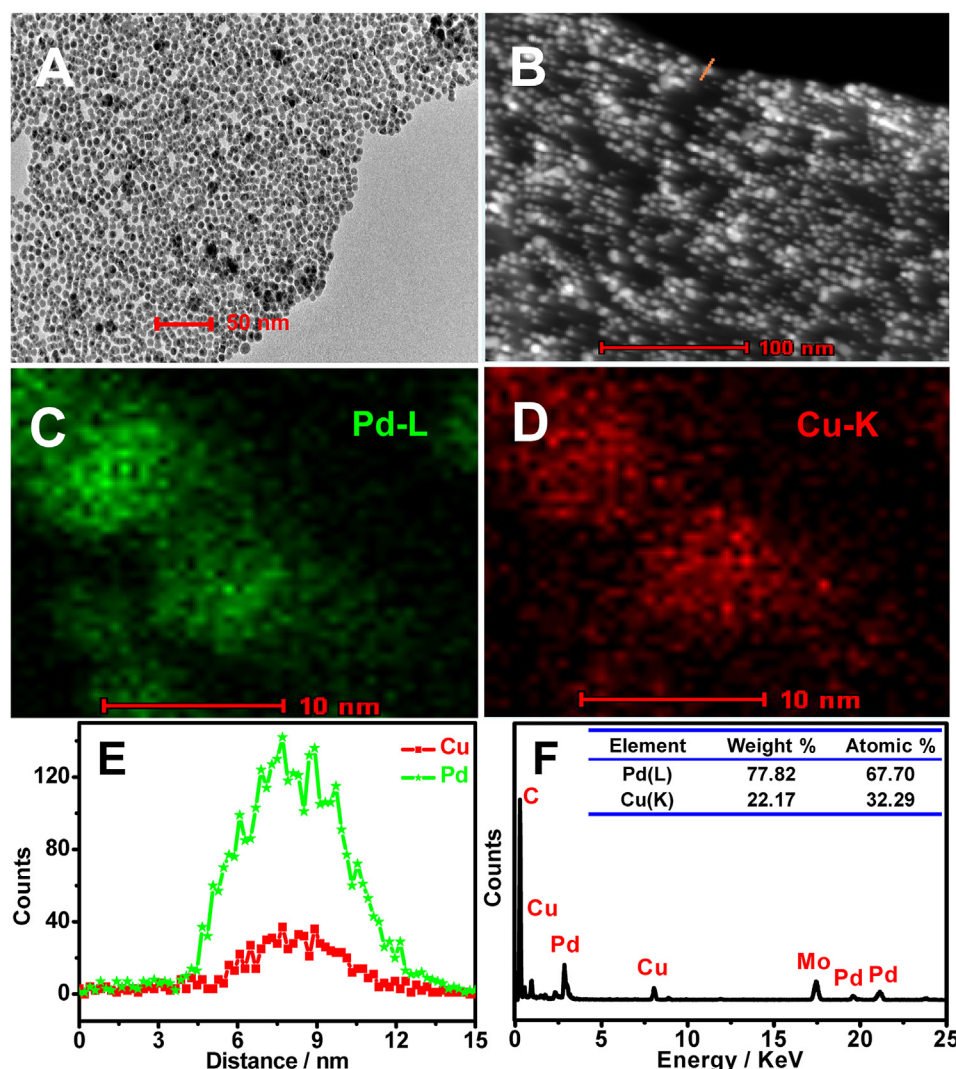


Fig. 1. TEM (A), HAADF-STEM (B), HAADF-STEM-EDS mapping images (C, D), line scanning profiles (E), and EDS spectrum (F) of Pd–Cu NCs/RGOs.

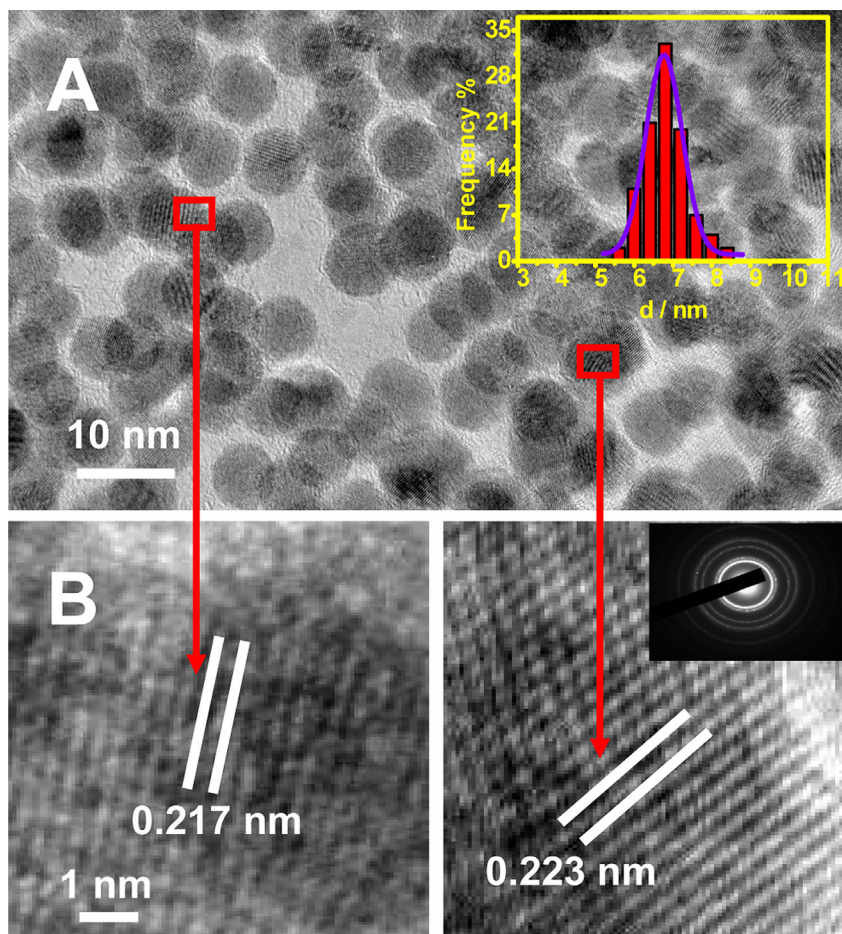


Fig. 2. HRTEM images (A, B) of Pd–Cu NCs/RGOs. Insets show the corresponding particle size distribution in (A) and SAED pattern in (B), respectively.

XPS spectra were recorded to verify the composition and surface chemical states of Pd–Cu NCs/RGOs [29]. As expected, Pd–Cu NCs/RGOs mainly contain Pd, Cu, C, and O elements (Fig. 4A). High-resolution C1s XPS spectrum is deconvoluted into four components (Fig. 4B), which can be assigned to C–C (284.5 eV), C–O (285.7 eV), C=O (287.5 eV), and O–C=O (288.0 eV) bonds [22], respectively. The C–C bonds are the predominant species by measuring the relative peak areas, indicating the deoxygenation of GOs during the solvothermal procedure [23]. The predominant Pd⁰ 3d_{5/2} and Pd⁰ 3d_{3/2} peaks can be observed in high-resolution Pd 3d XPS spectrum of Pd–Cu NCs/RGOs (Fig. 4C), revealing complete reduction of Pd(acac)₂ in the present synthesis [39].

With respect to Cu valence states, the Cu 2p and Cu LMM XPS spectra were both provided (Fig. 4D). The higher intensity peaks located at 931.8 and 951.8 eV correspond to Cu⁰, while the weaker ones at 944.1 and 962.6 eV are the characteristic peaks of Cu²⁺ in the form of CuO [40]. Besides, the Cu LMM Auger peak at 918.7 eV (inset in Fig. 4D) is consistent with Cu⁰ [17]. These results evidence the coexistence of Cu⁰ and Cu²⁺ in Pd–Cu NCs/RGOs, but the amount of Cu⁰ is slightly higher than that of Cu²⁺ [8].

TGA curves (Fig. 5) were obtained to analyze the thermal stability of Pd–Cu NCs/RGOs, and evaluate the mass loading of Pd–Cu NCs on RGOs. For the sample of GOs, the weight loss within 100 °C comes from water evaporation. The weight loss in the temperature range of 150–250 °C is ascribed to the decomposition of oxygen-containing functional groups, and the weight loss above 500 °C is attributed to the combustion of carbon skeleton [37]. Evidently, the weight loss of Pd–Cu NCs/RGOs (curve a) is much slower from

room temperature to 900 °C, which is different from that of GOs (curve b) under the identical conditions, indicating the decreased quantity of the oxygenated functional groups on RGOs [41]. This result further confirms the efficient reduction of GOs to RGOs [42]. Additionally, the mass loading is about 70.8 wt % for Pd–Cu NCs on RGOs [43].

The ECSA of Pd–Cu NCs/RGOs (Fig. 6A, curve a) and Pd black (Fig. 6A, curve b) modified electrodes were measured based on the CO-stripping measurements [44]. The ECSA is about 49.2 m² g^{−1} for Pd–Cu NCs/RGOs, which is much larger than those of commercial Pd black (4.8 m² g^{−1}) and nanoporous NP–Pd₅₀Cu₅₀ alloy (28.0 m² g^{−1}) [33], implying the enhanced electrocatalytic activity of Pd–Cu NCs/RGOs. On the other hand, the onset potential of Pd–Cu NCs/RGOs is obviously more negative than that of Pd black, verifying that the existence of Cu can facilitate the removal of poisoning intermediate species such as CO, and thus improve the catalytic property of Pd–Cu NCs/RGOs [45].

The electrocatalytic activity of Pd–Cu NCs/RGOs was investigated toward ORR, which includes both the breaking of the O–O bond and the formation of the OH bond [29]. A group of linear sweep voltammograms (LSVs) were recorded in alkaline media, using Pd black and RGOs as references. Fig. 7A displays the LSVs of Pd–Cu NCs/RGOs (curve a), Pd black (curve b) and RGOs (curve c) modified electrodes. Obviously, the onset potential and half-wave potential of Pd–Cu NCs/RGOs are much more positive than those of Pd black, RGOs, and the Au–Pd nanostructures in the previous report [46]. Additionally, the current density of Pd–Cu NCs/RGOs is larger than those of Pd black and RGOs in the whole potential range.

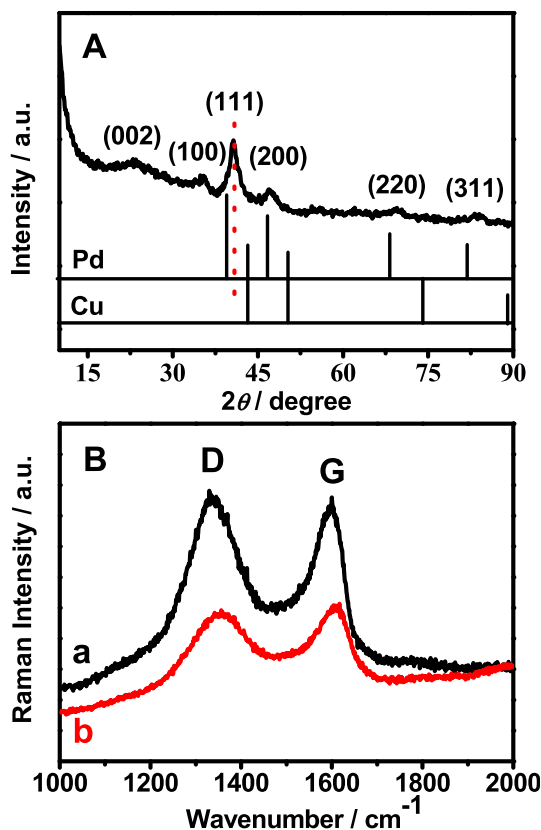


Fig. 3. XRD (A) and Raman (B) spectra of Pd–Cu NCs/RGOs (curve a) and GOs (curve b).

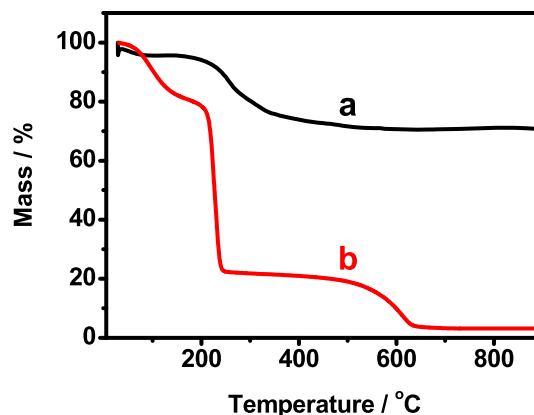


Fig. 5. TGA curves of Pd–Cu NCs/RGOs (curve a) and GOs (curve b).

Furthermore, the corresponding current densities were normalized with the same mass at the potential of -0.26 V (vs. RHE), in which Pd–Cu NCs/RGOs show about 38.4 mA mg^{-1} , much higher than those of Pd black (15.7 mA mg^{-1}) and RGOs (2.07 mA mg^{-1}). Taken together, the above results reveal the improved electrocatalytic performance of Pd–Cu NCs/RGOs toward ORR, which can be attributed to the addition of Cu varying the Pd electronic structure and the presence of RGOs improving the mass transport [25,47].

The stability of a catalyst is of great importance for its commercial applications in fuel cells [48]. The stability of Pd–Cu NCs/RGOs for ORR was investigated using LSVs recorded between -0.8 and 0 V for 1000 cycles with a scan rate of 5 mV s^{-1} in O_2 -saturated 0.1 M KOH . As shown in Fig. 7B, there is only about 14 mV positive-shift at the half-wave potential, much less variation than that of Pt@PdCu₅/C (65 mV negative-shift) [8].

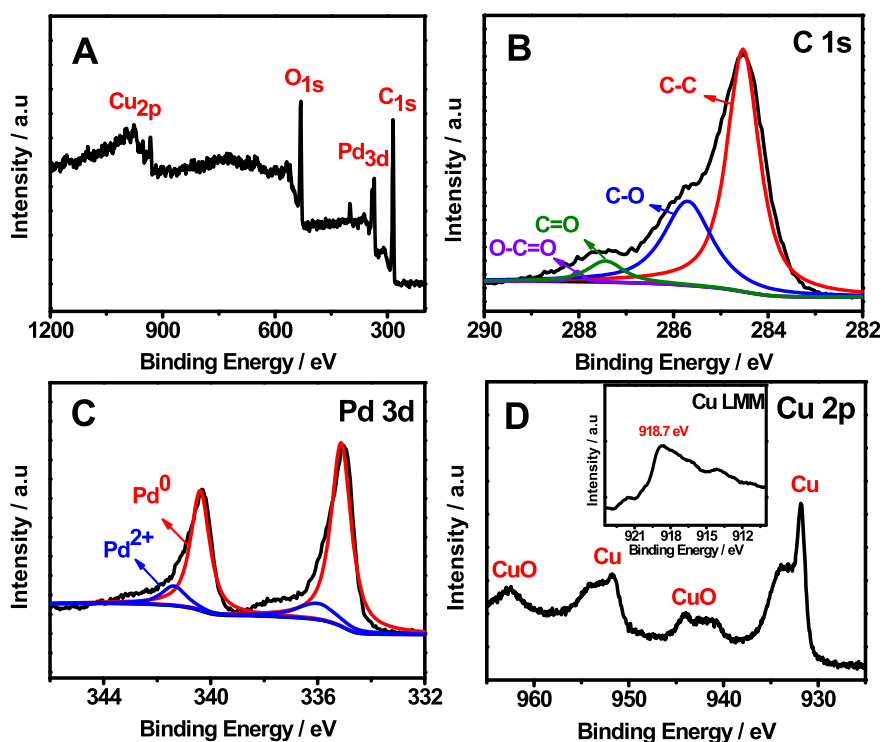


Fig. 4. Survey (A), and high-resolution C 1s (B), Pd 3d (C), and Cu 2p (D) XPS spectra of Pd–Cu NCs/RGOs. Inset in (D) shows the Cu LMM Auger spectrum.

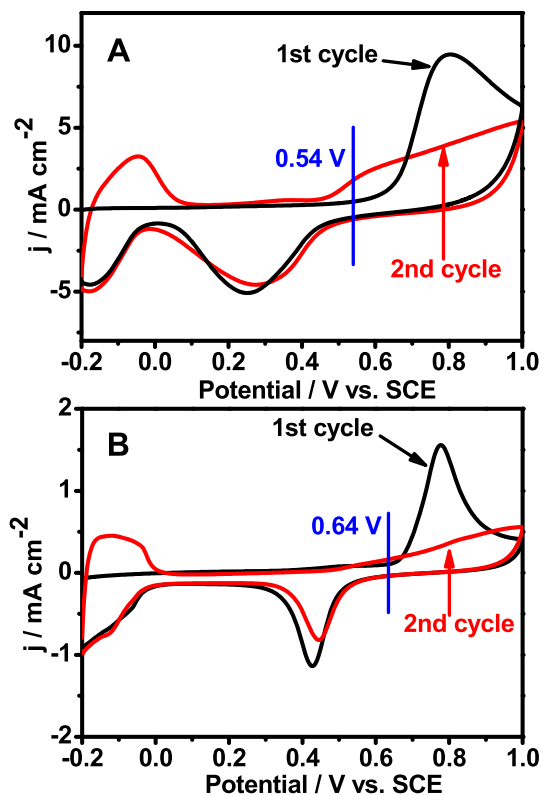


Fig. 6. CO-stripping voltammograms of Pd–Cu NCs/RGOs (A) and commercial Pd black (B) modified electrodes in 0.5 M H_2SO_4 at the scan rate of 50 mV s^{-1} .

Simultaneously, the diffusion-limiting current density exhibits nearly no change after 1000 cycles, similar to $\text{Pt}_{0.5}\text{Cu}_{1/2}$ NCs for ORR stability in the literature [31]. These phenomena evidence that Pd–Cu NCs/RGOs own long-term durability toward ORR [29].

The polarization curves were obtained on the Pd–Cu NCs/RGOs modified electrode toward O_2 reduction with different rotating rates to evaluate the ORR pathway (Fig. 7C). The current densities increase with the increase of the rotating rates, due to the rapid diffusion of O_2 molecules to the electrode surface [49]. Meanwhile, the diffusion-limiting current densities were analyzed by Koutecky–Levich (K–L) equation [19] at the potentials of -0.4 and -0.6 V , and the K–L plots were provided (Fig. 7D). According to the corresponding slopes, the electron transfer number (n) is estimated to be 4.03 and 3.87 at the potentials of -0.4 and -0.6 V , respectively, suggesting a direct reduction of O_2 to H_2O via the 4-electron pathway [10,19].

The alcohol-tolerant activity of a cathodic electrocatalyst is critical for its development in fuel cells, because the permeation of methanol from anode side causes a mixed potential at the cathode side to damage the cell [50]. To assess the alcohol tolerant ability of Pd–Cu NCs/RGOs, Pd black, and RGOs modified electrodes, the cyclic voltammograms (CVs) were recorded with and without 3 M methanol in 0.1 M KOH (Fig. 8). The Pd–Cu NCs/RGOs (Fig. 8A) and RGOs (Fig. 8B) modified electrodes display negligible catalytic current in the presence of 3.0 M methanol, compared to Pd black (Fig. 8C). This observation demonstrates that Pd–Cu NCs/RGOs is methanol tolerant and selectively sensitive to ORR from methanol in alkaline media [51,52].

4. Conclusion

In conclusion, well-defined monodisperse bimetallic alloyed Pd–Cu NCs were uniformly decorated on RGOs by a facile one-pot solvothermal strategy, with the average size of 6.81 nm, endowing it with enlarged ECSA. The as-prepared nanocomposites showed highly enhanced electrocatalytic activity, long-term stability, and remarkable methanol-tolerance ability for ORR in alkaline media. The outstanding electrocatalytic property would make it a promising candidate for a variety of catalysis in fuel cells and others.

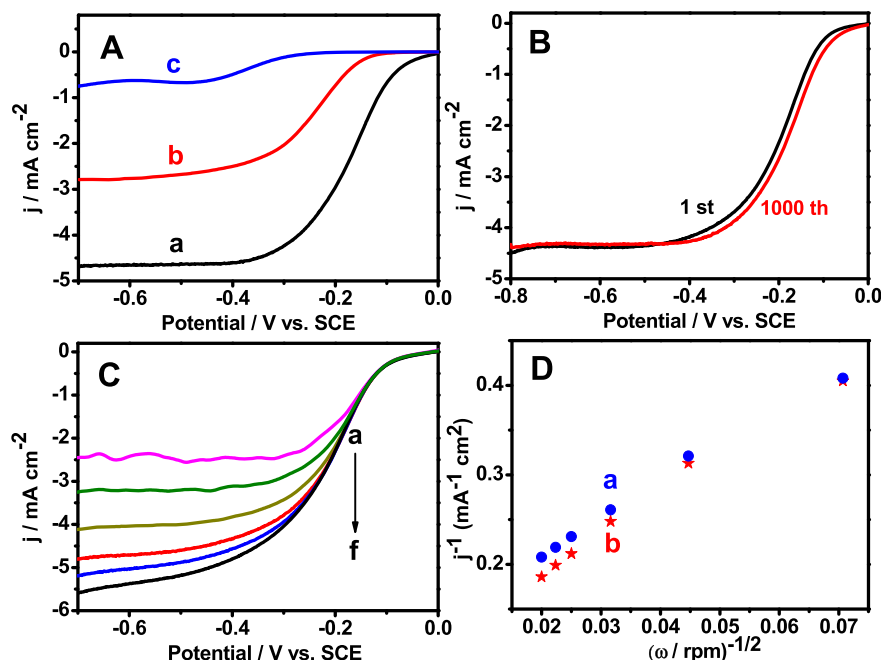


Fig. 7. LSVs (A) of Pd–Cu NCs/RGOs (curve a), commercial Pd black (curve b) and RGOs (curve c) modified electrodes in O_2 -saturated 0.1 M KOH with the scan rate of 5 mV s^{-1} and rotation rate of 1600 rpm. LSVs (B) of Pd–Cu NCs/RGOs before and after 1000 cycles. LSVs (C) of Pd–Cu NCs/RGOs modified electrode with different rotating rates: 200, 500, 900, 1000, 2000, and 2500 rpm. The corresponding K–L plots (D) at -0.4 (curve a) and -0.6 V (curve b).

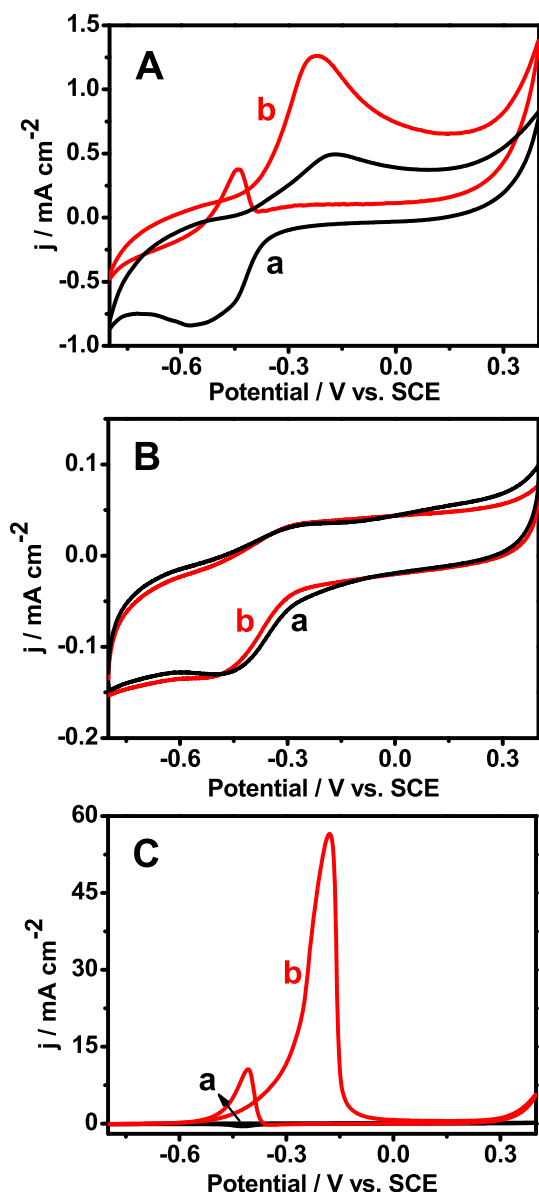


Fig. 8. CVs of Pd–Cu NCs/RGOs (A), RGOs (B), and Pd black (C) modified electrodes without (curve a) and with (curve b) 3.0 M methanol in 0.1 M KOH at the scan rate of 50 mV s⁻¹.

Acknowledgments

This work was financially supported by the NSFC (21175118, 21275130, 21275131 and 11304286) and Zhejiang Province University young academic leaders of academic climbing project (No. pd2013055).

References

- [1] B. Wu, Y. Kuang, X. Zhang, J. Chen, *Nano Today* 6 (2011) 75–90.
- [2] H. Zhang, M. Jin, Y. Xia, *Angew. Chem. Int. Ed.* 51 (2012) 7656–7673.
- [3] X. Yang, Q. Yang, J. Xu, C.-S. Lee, *J. Mater. Chem.* 22 (2012) 8057–8062.
- [4] W. Zhang, M. Wang, J. Chen, T. Romeo, A.T. Harris, A.I. Minett, *Electrochim. Commun.* 34 (2013) 73–76.
- [5] C. Zhu, S. Guo, S. Dong, *Chem. Eur. J.* 19 (2013) 1104–1111.
- [6] M. Liu, Y. Lu, W. Chen, *Adv. Funct. Mater.* 23 (2013) 1289–1296.

- [7] K.-H. Park, Y.W. Lee, Y. Kim, S.W. Kang, S.W. Han, *Chem. Eur. J.* 19 (2013) 8053–8057.
- [8] T. Cochell, A. Manthiram, *Langmuir* 28 (2011) 1579–1587.
- [9] F. Gopal, R. Arab, *J. Electroanal. Chem.* 647 (2010) 66–73.
- [10] J.-N. Zheng, S.-S. Li, X. Ma, F.-Y. Chen, A.-J. Wang, J.-R. Chen, J.-J. Feng, *J. Power Sources* 262 (2014) 270–278.
- [11] J.-H. Jang, C. Pak, Y.-U. Kwon, *J. Power Sources* 201 (2012) 179–183.
- [12] Y. Pan, F. Zhang, K. Wu, Z. Lu, Y. Chen, Y. Zhou, Y. Tang, T. Lu, *Int. J. Hydrogen Energy* 37 (2012) 2993–3000.
- [13] C.-H. Cui, J.-W. Yu, H.-H. Li, M.-R. Gao, H.-W. Liang, S.-H. Yu, *ACS Nano* 5 (2011) 4211–4218.
- [14] M.H. Shao, T. Huang, P. Liu, J. Zhang, K. Sasaki, M.B. Vukmirovic, R.R. Adzic, *Langmuir* 22 (2006) 10409–10415.
- [15] K.N. Heck, B.G. Janesko, G.E. Scuseria, N.J. Halas, M.S. Wong, *J. Am. Chem. Soc.* 130 (2008) 16592–16600.
- [16] L. Xiao, L. Zhuang, Y. Liu, J. Lu, H.D. Abruna, *J. Am. Chem. Soc.* 131 (2008) 602–608.
- [17] S.C. Tang, X.K. Meng, S. Vongehr, *Electrochim. Commun.* 11 (2009) 867–870.
- [18] X.-R. Li, X.-L. Li, M.-C. Xu, J.-J. Xu, H.-Y. Chen, *J. Mater. Chem. A* 2 (2014) 1697–1703.
- [19] C. Wang, H. Daimon, T. Onodera, T. Koda, S. Sun, *Angew. Chem. Int. Ed.* 47 (2008) 3588–3591.
- [20] B. Lim, M. Jiang, P.H.C. Camargo, E.C. Cho, J. Tao, X. Lu, Y. Zhu, Y. Xia, *Science* 324 (2009) 1302–1305.
- [21] J. Han, Z. Zhou, Y. Yin, X. Luo, J. Li, H. Zhang, B. Yang, *CrystEngComm* 14 (2012) 7036–7042.
- [22] J.-J. Lv, S.-S. Li, J.-N. Zheng, A.-J. Wang, J.-R. Chen, J.-J. Feng, *Int. J. Hydrogen Energy* 39 (2014) 3211–3218.
- [23] S.-S. Li, J.-J. Lv, Y.-Y. Hu, J.-N. Zheng, J.-R. Chen, A.-J. Wang, J.-J. Feng, *J. Power Sources* 247 (2014) 213–218.
- [24] K.S. Novoselov, A.K. Geim, S.V. Morozov, D. Jiang, Y. Zhang, S.V. Dubonos, I.V. Grigorieva, A.A. Firsov, *Science* 306 (2004) 666–669.
- [25] S. Zhang, Y. Shao, H.-G. Liao, J. Liu, I.A. Aksay, G. Yin, Y. Lin, *Chem. Mater.* 23 (2011) 1079–1081.
- [26] D. Chen, L. Tang, J. Li, *Chem. Soc. Rev.* 39 (2010) 3157–3180.
- [27] W.S. Hummers, R.E. Offeman, *J. Am. Chem. Soc.* 80 (1958) 1339–1339.
- [28] D.-L. Zhou, J.-J. Feng, L.-Y. Cai, Q.-X. Fang, J.-R. Chen, A.-J. Wang, *Electrochim. Acta* 115 (2014) 103–108.
- [29] G. Fu, K. Wu, J. Lin, Y. Tang, Y. Chen, Y. Zhou, T. Lu, *J. Phys. Chem. C* 117 (2013) 9826–9834.
- [30] C.-K. Tsung, J.N. Kuhn, W. Huang, C. Aliaga, L.-I. Hung, G.A. Somorjai, P. Yang, *J. Am. Chem. Soc.* 131 (2009) 5816–5822.
- [31] M. Wang, W. Zhang, J. Wang, A. Minett, V. Lo, H. Liu, J. Chen, *J. Mater. Chem. A* 1 (2013) 2391–2394.
- [32] G. Fu, X. Jiang, M. Gong, Y. Chen, Y. Tang, J. Lin, T. Lu, *Nanoscale* 6 (2014) 8226–8234.
- [33] C. Xu, A. Liu, H. Qiu, Y. Liu, *Electrochim. Commun.* 13 (2011) 766–769.
- [34] Z.-L. Wang, J.-M. Yan, H.-L. Wang, Y. Ping, Q. Jiang, *J. Mater. Chem. A* 1 (2013) 12721–12725.
- [35] L. Xiong, Y.-X. Huang, X.-W. Liu, G.-P. Sheng, W.-W. Li, H.-Q. Yu, *Electrochim. Acta* 89 (2013) 24–28.
- [36] Y. Zhao, L. Zhan, J. Tian, S. Nie, Z. Ning, *Electrochim. Acta* 56 (2010) 1967–1972.
- [37] J. Li, W. Tang, J. Huang, J. Jin, J. Ma, *Catal. Sci. Technol.* 3 (2013) 3155–3162.
- [38] R.N. Singh, R. Awasthi, *Catal. Sci. Technol.* 1 (2011) 778–783.
- [39] S.-S. Li, J. Yu, Y.-Y. Hu, A.-J. Wang, J.-R. Chen, J.-J. Feng, *J. Power Sources* 254 (2014) 119–125.
- [40] M. Grouchko, A. Kamysny, S. Magdassi, *J. Mater. Chem.* 19 (2009) 3057–3062.
- [41] F. Li, Y. Guo, R. Li, F. Wu, Y. Liu, X. Sun, C. Li, W. Wang, J. Gao, *J. Mater. Chem. A* 1 (2013) 6579–6587.
- [42] M. Sawangphruk, A. Kritayavathananon, N. Chinwipras, *J. Mater. Chem. A* 1 (2013) 1030–1034.
- [43] T.T. Dang, V.H. Pham, B.K. Vu, S.H. Hur, E.W. Shin, E.J. Kim, J.S. Chung, *Mater. Lett.* 86 (2012) 161–164.
- [44] C. Hu, Z. Bai, L. Yang, J. Lv, K. Wang, Y. Guo, Y. Cao, J. Zhou, *Electrochim. Acta* 55 (2010) 6036–6041.
- [45] Y. Wang, Z.M. Sheng, H. Yang, S.P. Jiang, C.M. Li, *Int. J. Hydrogen Energy* 35 (2010) 10087–10093.
- [46] L. Kuai, X. Yu, S. Wang, Y. Sang, B. Geng, *Langmuir* 28 (2012) 7168–7173.
- [47] J.W. Hong, D. Kim, Y.W. Lee, M. Kim, S.W. Kang, S.W. Han, *Angew. Chem.* 123 (2011) 9038–9042.
- [48] C. Hsu, C. Huang, Y. Hao, F. Liu, *Phys. Chem. Chem. Phys.* 14 (2012) 14696–14701.
- [49] Z. Jiang, Z.-J. Jiang, X. Tian, W. Chen, *J. Mater. Chem. A* 2 (2014) 441–450.
- [50] S. An, J.-H. Park, C.-H. Shin, J. Joo, E. Ramasamy, J. Hwang, J. Lee, *Carbon* 49 (2011) 1108–1117.
- [51] W. He, J. Liu, Y. Qiao, Z. Zou, X. Zhang, D.L. Akins, H. Yang, *J. Power Sources* 195 (2010) 1046–1050.
- [52] Y. Tan, C. Xu, G. Chen, N. Zheng, Q. Xie, *Energy Environ. Sci.* 5 (2012) 6923–6927.